Article

Structure and Mixed Proton-Electronic Conductivity in PR-Substituted La5.4MoO12- Ceramics

Abraham Sánchez-Caballero , José M. Porras-Vázquez [*] , Lucía dos Santos-Gómez , Javier Zamudio-García , Antonia Infantes-Molina , Jesús Canales-Vázquez , Enrique R. Losilla , David Marrero-López [*]

Article

Structure and Mixed Proton-Electronic Conductivity in Pr-Substituted La$_{5.4}$MoO$_{12-\delta}$ Ceramics

Abraham Sánchez-Caballero [1], José M. Porras-Vázquez [1,*], Lucía dos Santos-Gómez [1], Javier Zamudio-García [2], Antonia Infantes-Molina [1], Jesús Canales-Vázquez [3], Enrique R. Losilla [1] and David Marrero-López [4,*]

[1] Universidad de Málaga, Dpto. de Química Inorgánica, Cristalografía y Mineralogía 29071-Málaga, Spain; josema@uma.es
[2] Department of Energy Conversion and Storage, Technical University of Denmark, Fysikvej, 310, 2800, Kgs., Lyngby, Denmark
[3] Renewable Energy Research Institute, Escuela Técnica Superior de Ingenieros Industriales de Albacete, University of Castilla-La Mancha, 02071, Albacete, Spain
[4] Universidad de Málaga, Dpto. de Física Aplicada I, 29071-Málaga, Spain; marrero@uma.es
* Correspondence: josema@uma.es (JMPV), marrero@uma.es (DML)

Abstract: Lanthanide molybdates, with the general formula Ln$_{5.4}$MoO$_{11.1-\delta}$, are materials known for their mixed proton-ionic conductivity. This study investigated the effects of Pr content and Nb-doping on the crystal structure and electrical properties of the La$_{5.4-x}$Pr$_x$Mo$_{1-y}$Nb$_y$O$_{12-\delta}$ (x= 0, 1.35, 2.7, 4.05, 5.4; y= 0, 0.1) series. The research focuses on two primary objectives: (i) enhancing the electronic conductivity through the use of Pr^{4+}/Pr^{3+} redox pairs, and (ii) increasing the ionic conductivity through Nb^{5+} aliovalent doping. The materials were thoroughly characterized by X-ray powder diffraction (XRD), X-ray photoelectron spectroscopy (XPS), transmission and scanning electron microscopy (TEM and SEM), and complex impedance spectroscopy. The average crystal structure of the materials depends significantly on the Pr content. In general, compositions with higher Pr content crystallize in a cubic fluorite-type structure, whereas lower Pr content stabilizes a rhombohedral polymorph. However, detailed TEM studies reveal a more complex local crystal structure characterized by nanodomains and incommensurate modulations. The highest conductivity values are observed in a N$_2$ atmosphere for compositions with elevated Pr content, attributed to electronic conduction mediated by the Pr^{4+}/Pr^{3+} redox pair, as confirmed by XPS. These findings highlight the potential of tailored doping strategies to optimize the conducting properties of lanthanide molybdates for specific high-temperatures electrochemical applications.

Keywords: La$_{5.4}$MoO$_{12-\delta}$; polymorphism; mixed ionic-electronic conductivity

1. Introduction

High temperature proton conducting ceramics have a wide range of industrial applications due to their exceptional thermal stability, chemical resistance, and mechanical strength. They are commonly used as gas sensor, electrolytes in solid oxide fuel cell and electrolyzers, as well as membranes for hydrogen separation and purification [1–5].

BaCeO$_3$ and BaZrO$_3$ perovskites are among the most commonly studied materials membranes for hydrogen separation due to their high proton conductivity [6–8]. However, BaCeO$_3$ suffers for low chemical stability in H$_2$O and CO$_2$ environments, while BaZrO$_3$ despite its improved stability, requires very high sintering temperatures to achieve the desired level of densification. To combine the properties of both materials, BaCe$_{1-x}$Zr$_x$O$_3$ compositions have been investigated. These materials have been optimized through appropriate doping with Yb and Y, with the composition BaZr$_{0.2}$Ce$_{0.6}$Y$_{0.1}$Yb$_{0.1}$O$_3$ showing the highest proton conductivity values for fuel cell application [9]. However. the high basicity of Ba remains a drawback for application of these materials in CO$_2$ rick

environments [10].   For this reason, alternative proton conductors without alkaline earth elements, such as $La_2Ce_2O_7$ and $LaNbO_4$ have been investigated [11–13].

Lanthanum tungstates, $La_{6-x}WO_{12-\delta}$, have emerged as promising proton-conducting materials with tunable properties for both fuel cell electrolytes and ceramic hydrogen separation membranes due to their chemical stability, as well as their resistance to gases such as H_2S, CO and CO_2 [14–17]. A strategy for enhancing the electronic conductivity of these materials consists of partially or completely substituting tungsten with molybdenum, resulting in $La_{6-x}MoO_{12-\delta}$ compounds, which exhibit higher electronic conductivity due to the easier reducibility of Mo^{6+} compared to W^{6+} [18–20].

In recent years, our research group has investigated the relationship between composition and synthesis-sintering conditions in lanthanum molybdates, leading to tunable structural and electrical properties [21,22]. The $La_{6-x}MoO_{12-\delta}$ series ($0 \le x \le 3$) was synthesized using the freeze-drying method, where the precursors were heated to 1500 ℃ and subsequently cooled at different rates. Samples that were rapidly cooled from 1500 ℃ exhibited a disordered cubic fluorite symmetry. However, at lower cooling rates and for high lanthanum contents ($x \le 1$), two different ordered rhombohedral polymorphs were observed: one with a 7×7×1 superstructure relative to a disordered cubic fluorite denoted as R1; and another with a 5×5×1 superstructure denoted as R2. The crystal structures were satisfactorily determined using a combination of HRTEM images and SAED patterns, employing the De Wolff's theory and the Rietveld method with neutron powder diffraction data. For lower lanthanum contents, $1.5 \le x \le 3$, the cubic symmetry was favored at high sintering temperatures (1400-1500 ℃) and rapid cooling (5 ℃ min^{-1}), while a monoclinic polymorph [23] was obtained at lower sintering temperatures (1100-1300 ℃) and very slow cooling (0.5 ℃ min^{-1}).

The preparation conditions and composition significantly influence the electrical properties of lanthanum molybdates. A decrease in ionic conductivity was observed as the La/Mo ratio decreased; however, this was accompanied by an increase in electronic conductivity, significantly enhanced under reducing conditions (5% H_2-Ar) [24]. Furthermore, the symmetry and electrical properties of the samples can be tailored through aliovalent substitution of Mo^{6+} by Nb^{5+}, resulting in the stabilization of the R1 polymorph and an improved ionic conductivity due the generation of additional oxide ion vacancies [24].

On the other hand, Shlyakhtina *et al*. [25,26] have also studied the structural and electrical properties of molybdates with lanthanides smaller than lanthanum, $Ln_{5.5}MoO_{12-\delta}$, which exhibit different symmetries depending on the ionic radius of the lanthanide. They observed a fluorite-type cubic structure for Ln = Sm^{3+}, Gd^{3+}, and Dy^{3+} (s.g. $Fm\overline{3}m$); and a cubic bixbiite type for Ln = Ho^{3+}, Er^{3+}, Tm^{3+}, Yb^{3+}, and Lu^{3+} (s.g. $Ia\overline{3}$), noting a decrease in total conductivity as the size of the lanthanide decreases. In our research group we also have conducted a comprehensive investigation into the relationship between structural and electrical properties and synthesis-sintering conditions for middle-size lanthanides, $Ln_{5.4}MoO_{11.1}$ (Ln = Nd^{3+}, Sm^{3+} and Gd^{3+}) [27]. As the lanthanide size decreases, the cubic symmetry is favored even at very low cooling rates, likely due to a smaller size mismatch between the lanthanide and molybdenum. Electrical property analysis also revealed lower ionic conductivity for smaller lanthanides, but a significant enhancement in the electronic conductivity in reducing conditions.

Continuing the research on this family of proton conductors, the primary aim of this study is to investigate the influence of Pr-doping in $La_{5.4}MoO_{11.1}$ to enhance the electronic conductivity. This is motivated by the known effect of the Pr^{4+}/Pr^{3+} pair in conferring a significant electronic conductivity in energy-applied materials [28,29]. Additionally, it has been reported that Nb^{5+}-doping at the W^{6+}/Mo^{6+} site in lanthanum tungstates/molybdates creates oxide vacancies, thereby enhancing ionic conductivity [24,30]. The materials were thoroughly characterized using X-ray powder diffraction, X-ray photoelectron spectroscopy, transmission and scanning electron microscopy and impedance spectroscopy under different gas-flowing atmospheres to evaluate their potential as ceramic membranes for hydrogen separation.

2. Materials and Methods

2.1. Synthesis

$La_{5.4-x}Pr_xMo_{1-y}Nb_yO_{12-\delta}$ samples (x = 1.35, 2.7. 4.05, 5.4; y = 0, 0.1) were synthesized using a freeze-drying precursor method, following the synthetic procedure described in a previous study for related compositions [21]. The starting reagents used were La_2O_3 (99.99%, Merck), Pr_6O_{11} (99.9%, Merck), MoO_3 (99.5%, Merck) and $Nb(HC_2O_4)_5 \cdot H_2C_2O_4$ (97%, ABCR). Precursor solutions were prepared by dissolving stoichiometric amounts of La_2O_3 and Pr_6O_{11} in diluted nitric acid, MoO_3 in diluted ammonia and $Nb(HC_2O_4)_5 \cdot H_2C_2O_4$ in water. Ethylenediaminetetraacetic acid (EDTA 99.99%, Merck) was added as a chelating agent in a 1:1 metal-to-EDTA ratio. The different cation solutions were mixed under stirring to obtain transparent solutions with a concentration of approximately 0.1 mol L^{-1} and a pH of 7. The solutions were frozen in liquid nitrogen and dehydrated by vacuum sublimation in a Scanvac-Coolsafe freeze-dryer for 2 days. The dried precursor powders were calcined at 300 ℃ for 1 h to partially decompose the solid precursors, followed by calcination at 800 ℃ for 1 h to completely remove the carbonaceous species. The resulting powders were pressed into pellets with a diameter of 10 mm and a thickness of 1 mm, then sintered at 1500 ℃ for 1 h with a heating rate of 10 ℃ min^{-1}, followed by cooling at three different rates: quenching (Q), 5 and 0.5 ℃ min^{-1}. The choice of cooling rate is critical as it can tailor the final crystal symmetry and electrical properties of the samples. Some of the obtained pellets were ground into powder for structural studies. Hereafter, all samples are labelled as $La_{5.4-x}Pr_xNb_y\_C$, where x and y represent the Pr and Nb content, respectively, and *C* denotes the cooling rate employed.

2.2. Structural and Microstructural Characterization

The purity and structure of the samples were analysed using laboratory X-ray powder diffraction with a PANalytical Empyrean diffractometer equipped with $CuK\alpha_{1,2}$ radiation, and a X'Pert Pro MPD (PANalytical) with $CuK\alpha_1$ radiation. The measurements were collected over a 2θ angular range of 10-80º with an acquisition time of 1 h. Phase identification was performed using the X'Pert HighScore Plus software [31], and structural analysis was carried out with the GSAS software [32].

X-ray photoelectron spectroscopy measurements were recorded using a Scienta ESCA 200 spectrometer with a monochromatic X-ray Al(Kα) source (1486.6 eV), operating under an ultra-high vacuum of 10^{-10} mbar. The experimental methodology for XPS included a full width at half maximum of 0.65 eV for the Au $4f_{7/2}$ line. Data analysis was carried out using the Multipak-V9.3 software package [33]. A Shirley-type background was subtracted from the signals, and the recorded spectra were fitted using Gaussian−Lorentzian curves to more accurately determine the binding energy of the different element core levels.

Selected area electron diffraction (SAED) and high-resolution transmission electron microscopy (HRTEM) were employed to study the crystal structure of the materials. TEM specimens were prepared by suspending finely ground powders in acetone and depositing a drop of the mixture onto a holey-carbon Cu grid (EMS). The analysis was performed using a Jeol JEM 2100 electron microscope operating at 200 kV, equipped with a ±25º double-tilt sample holder. Images were analysed using the Digital Micrograph™ software from Gatan [34].

The morphology and cation composition of the ceramic pellets were examined using field emission scanning electron microscopy (FEI-SEM, Helios Nanolab 650), coupled with energy dispersive spectroscopy (EDS, Oxford Instruments). The grain size was determined from the SEM micrographs using the linear intercept method [35].

2.3. Electrical Characterization

The electrical conductivity was determined using impedance spectroscopy with a frequency response analyser (Solartron 1260 FRA) under dry and wet N_2 (2% vol. H_2O) and wet 5% H_2-Ar atmospheres. Measurements were conducted within the frequency range of 0.01 Hz to 1 MHz, applying an AC perturbation of 50 mV while cooling from 750 to 100 °C, with a dwell time of 30 min

at each measurement temperature. Pt current collectors were formed by coating the pellet surfaces with Pt-ink (METALOR® 6082) and firing at 800 °C for 1 h in air. The data were analysed using the ZView program [36].

3. Results

3.1. Phase Formation

X-ray diffraction patterns of the $La_{5.4-x}Pr_xMo_{1-y}Nb_yO_{12-\delta}$ series, heated at 1500 °C for 1 h and subsequently cooled at different rates, are shown in Figures S1 (quenched samples, Q) and Figure 1 (5 and 0.5 °C min^{-1} cooling rates). All the samples are single-phase compounds; however, the crystal symmetry is dependent on both the composition and cooling rate employed. Mo volatilization is considered negligible in these compounds, as reported previously for related compositions, based on EDS and Inductively Coupled Plasma measurements [37].

All quenched samples (Q), regardless of the composition, crystallize in a disordered cubic fluorite, similar to $La_{6-x}Mo_{1-y}Nb_yO_{12-\delta}$ (x = 0.6 – 3; y = 0 - 0.2) [21,22,24] and $Ln_{5.4}MoO_{11.1}$ (Ln = Nd, Sm and Gd) series [27], which were also rapidly cooled from 1500 °C. This behaviour can be attributed to the high thermal vibration of the atoms at 1500 °C, causing them to occupy the same atomic positions: (0, 0, 0) for the cations (La, Pr, Mo and Nb) and (¼, ¼, ¼) for the oxide anions, all within the $Fm\overline{3}m$ space group. Consequently, the quenching process preserves these atomic positions at room temperature, resulting in a high-symmetry cubic fluorite structure.

At lower cooling rates, such as 5 and 0.5 °C min^{-1}, thermodynamic factors become predominant, favouring the stabilization of the R1 rhombohedral polymorphs. This behaviour can be attributed to the varying ionic radii of the cations: 1.16, 1.02, 1.13, 0.96 and 0.74 Å for La^{3+}, Mo^{6+}, Pr^{3+}, Pr^{4+} and Nb^{5+}, respectively, all in an 8-fold coordination. This size mismatch, along with the lower cooling rates, allows the cations to settle into thermodynamically stable positions, leading to a greater distortion of the coordination spheres and, consequently, a decrease in symmetry. Under these cooling conditions, the cubic symmetry is stabilized as the praseodymium content increases (Figure 1), due to the smaller size of Pr^{4+} and Pr^{3+} compared to La^{3+}, which reduces distortions in the molybdenum coordination sphere. The transition from the rhombohedral to the cubic polymorph is gradual with increasing Pr-content. However, $La_{4.05}Pr_{1.35}\_5$, despite having an average cubic structure, shows broad diffraction peaks, suggesting some rhombohedral distortion. In contrast, $La_{2.7}Pr_{2.7}\_5$ exhibits a cubic structure with narrow diffraction peaks. For the samples cooled down at 0.5 °C min^{-1}, where thermodynamics effects are more pronounced, a higher Pr content is required for stabilizing the cubic phase. $La_{4.05}Pr_{1.35}\_0.5$ can still be considered R1, and $La_{2.7}Pr_{2.7}0.5$ also shows a significant rhombohedral distortion. Complete conversion to the cubic phase is only achieved for $La_{1.35}Pr_{4.05}\_0.5$.

Nb-doping also plays an important role in determining the final symmetry of the samples (Figure 1c,d). For instance, as mentioned earlier, $La_{2.7}Pr_{2.7}\_0.5$ exhibits a rhombohedral distortion, whereas $La_{2.7}Pr_{2.7}Nb_{0.1}\_0.5$, cooled at the same rate, crystallizes into a simple cubic fluorite structure with narrow diffraction peaks. A similar behaviour was observed in a previous work for $La_{5.4}MoO_{11.1}$ [24], where the undoped sample, cooled down at 0.5 °C min^{-1}, exhibited an R2 symmetry, while a 10% Nb-doping at the molybdenum site stabilized the R1 structure. This effect is likely due to the generation of oxide vacancies induced by the aliovalent doping, which influences the structural stability and symmetry of the materials.
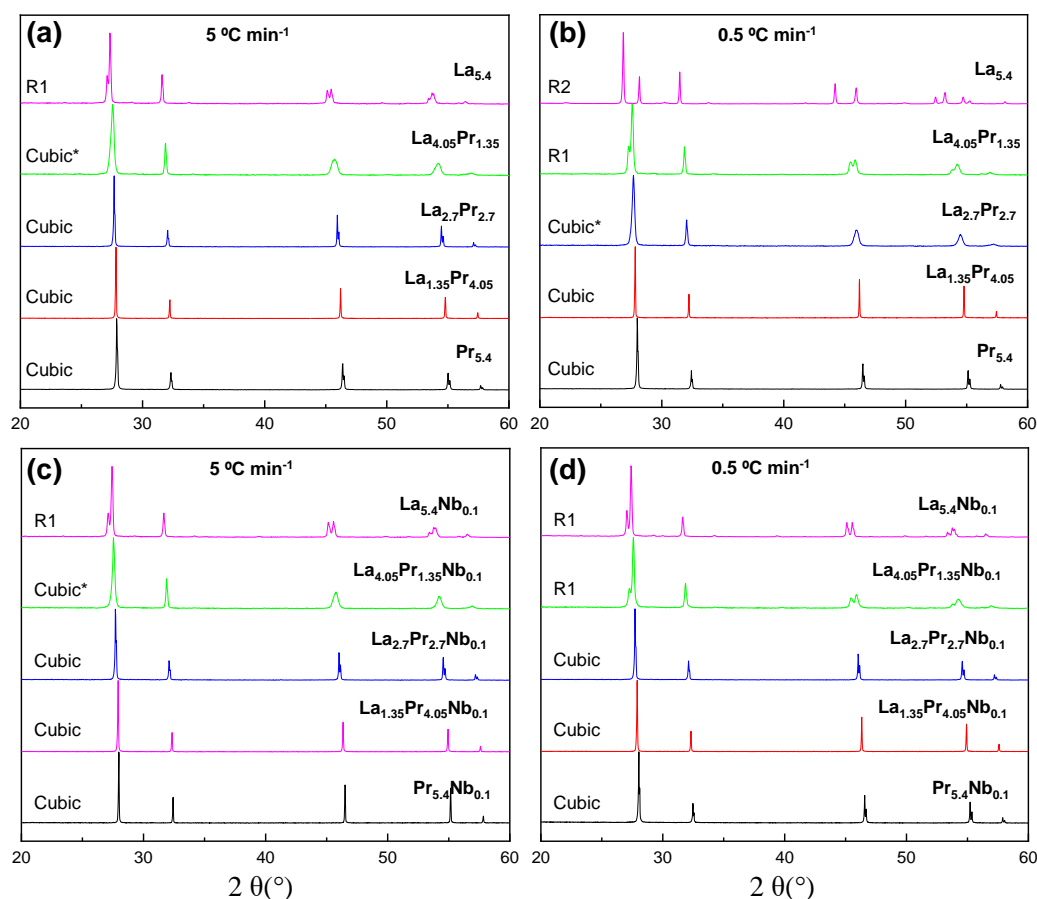
Figure 1. XRD patterns for $La_{5.4-x}Pr_xMo_{1-y}Nb_yO_{12-\delta}$ samples (x = 1.35, 2.7. 4.05, 5.4; y = 0, 0.1) heated at 1500 °C and cooled down at (a,c) 5 °C min^{-1} and (b,d) 0.5 °C min^{-1}. Symmetry of the samples is display within the figure. Several samples (*) exhibit broad diffraction peaks, suggesting a deviation from cubic symmetry.

3.2. Structural Analysis

The structural characterization of all samples was conducted using the Rietveld method. For the cubic compositions, a simple fluorite structural model was employed, where all cations (La, Mo, Pr and Nb) share the same crystallographic position. Occupancy factors were adjusted to match the theoretical compositions, and isotropic atomic displacement factors were constrained to a single value for consistency. The refinement process included fitting the unit cell, scale factor, background, peak shape coefficients and isotropic displacement parameters.

For the rhombohedral samples, which exhibit more complex crystal structures, a Le Bail analysis was performed using a $R\bar{3}$ space group. The structural models previously reported based on neutron powder diffraction [22] could not be used for X-ray diffraction studies, as X-ray radiation is less sensitive to oxygen ordering, which is critical for stabilizing the different polymorphs observed in these samples.

In general, the refinements exhibit very low disagreement factors, typically in the range of 5-12% for R_{ap} and 1-5% for R_F (Figure 2 and Table S1). Regardless of the cooling rate, the cell parameters decrease as the Pr content increases, with cell volume values of 45.51(1), 43.87(1) and 42.20(1) Å^3 for $La_{5.4}$_Q, $La_{2.7}Pr_{2.7}$_Q and $Pr_{5.4}$_Q, respectively. This reduction in cell volume is attributed to the smaller size of Pr^{3+}/Pr^{4+} (1.13 and 0.96 Å) compared to La^{3+} (1.16 Å). Additionally, Nb-doping results in decreased cell volumes for all cooling rates, due to the smaller size of Nb^{5+} (0.74 Å) compared to Mo^{6+} (1.02 Å). For instance, $La_{2.7}Pr_{2.7}$_Q and $La_{2.7}Pr_{2.7}Nb_{0.1}$_Q exhibit cell volumes of 43.87(1) and 43.67(1) Å^3, respectively. Finally, for a given composition, the highest cell volume is consistently observed for the quenched samples, with values of 43.87, 43.57 and 43.58 Å^3 for $La_{2.7}Pr_{2.7}$_Q, $La_{2.7}Pr_{2.7}$_5 and $La_{2.7}Pr_{2.7}$_0.5, respectively. This behaviour is possibly caused by the higher reducibility of Pr^{4+} at

elevated temperatures, leading to a higher amount of Pr^{3+} and thus an increase in the cell volumes. Conversely, at lower cooling rates, the formation of Pr^{4+} is favoured, resulting in decreased cell parameters.
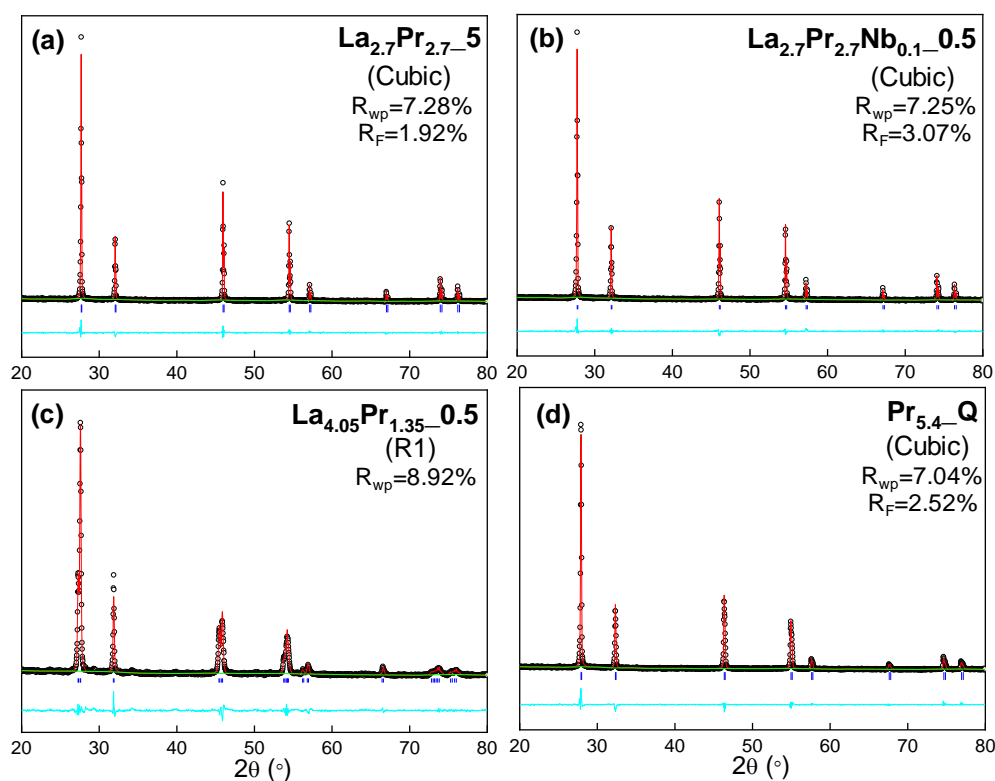
**Figure 2.** XRD Rietveld plots for (a) $La_{2.7}Pr_{2.7}5$, (b) $La_{2.7}Pr_{2.7}Nb_{0.1}5$, (c) $La_{4.05}Pr_{1.35}0.5$ and (d) $Pr_{5.4}Q$. Crystal system and agreement factors are displayed within the figure. [Observed data (crosses), calculated pattern (red continuous line), difference curve (cyan line) and reflection marks (blue short lines)].

After reduction of the samples in a 5% H_2-Ar flowing atmosphere at 800 °C for 24 h, most of the Pr^{4+} is potentially reduced to Pr^{3+}, resulting in an increase in cell volume that shows minimal variation regardless the cooling rate. For instance, $Pr_{5.4}\_Q$, $Pr_{5.4}\_5$ and $Pr_{5.4}\_0.5$ exhibit values after reduction of 42.91(1), 42.92(1) and 42.94(1) Å^3, respectively, higher than those for the as-prepared simples, 42.34(1), 42.03(1) and 41.99 (1) Å^3.

The local crystal structure was further examined using both electron diffraction (SAED) and HRTEM techniques. Figure 3a-c provides a comparative analysis of the SAED patterns obtained for selected compositions along the $[1\bar{1}0]$ zone axis. Samples with a high Pr-content ($Pr_{5.4}\_5$) exclusively present reflections corresponding to the cubic fluorite structure (Figure 3a). This identical SAED pattern persists in samples with lower Pr-content, such as $La_{2.7}Pr_{2.7}\_0.5$ (Figure 3b), despite the broad diffraction peaks observed by XRD (Figure 1).

Conversely, a completely different atomic arrangement is observed for $La_{2.7}Pr_{2.7}Nb_{0.1}\_0.5$ after Nb-doping (Figure 3c). The SAED patterns for these samples reveal additional diffraction reflections along specific crystallographic directions, notably [200] and [022]. This observation is consistent with an incommensurate modulation, as evidenced in previous studies using neutron diffraction data for related compositions [24]. Such an incommensurate structure is typically attributed to the local ordering of oxygen vacancies, likely induced by the aliovalent Nb-doping.
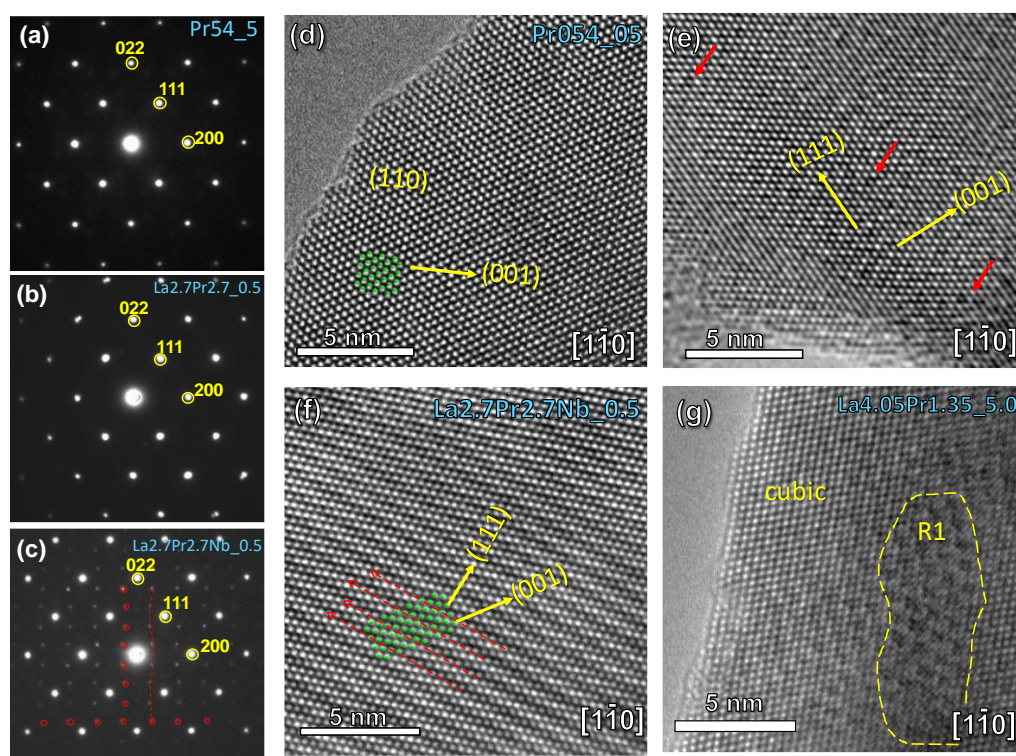
Figure 3. SAED patterns of (a) $Pr_{5.4}5$, (b) $La_{2.7}Pr_{2.7}0.5$ and (c) $La_{2.7}Pr_{2.7}Nb_{0.1}0.5$ in the $[1\bar{1}0]$ zone axis. HRTEM images of (d) $Pr_{5.4}0.5$, (e) $La_{2.7}Pr_{2.7}0.5$, (f) $La_{2.7}Pr_{2.7}Nb_{0.1}0.5$ and (g) $La_{4.05}Pr_{1.35}5$ in the $[1\bar{1}0]$ zone axis.

The HRTEM images corroborate the findings derived from the SAED analysis (Figure 3d-g). $Pr_{5.4}0.5$ exhibits an atomic arrangement consistent with a defect-free cubic fluorite structure (Figure 3d). However, as the Pr-content decreases, numerous local defects (marked by red arrows) become apparent, as observed in $La_{2.7}Pr_{2.7}\_0.5$ (Figure 3e). This defect-rich structure transforms into a modulated arrangement with Nb-doping due to the higher concentration of oxygen vacancies (Figure 3f). Finally, in the sample with the lowest Pr-content, $La_{4.05}Pr_{1.35}\_5$, a predominantly cubic fluorite structure is observed, interspersed with embedded microdomains of the R1 polymorph (Figure 3g). These microdomains explain the broad diffraction peaks observed in XRD patterns and the gradual symmetry transition observed as the Pr content increases (Figure 1).

3.3. XPS Analysis

Surface chemical state and atomic concentration information of the quenched samples in air were obtained from X-ray photoelectron spectroscopy. The Mo $3d$ core level spectra (Figure 4ab) consist of two doublets, Mo $3d_{5/2}$ and Mo $3d_{3/2}$. The predominant component, Mo $3d_{5/2}$, is located at 232.2 eV, characteristic of the Mo^{6+} species, as reported previously [21]. Additionally, a minor contribution at a higher binding energy (BE) of 233.3 eV is detected, also attributed to the Mo^{6+} species but in different chemical environments. After Nb doping, the same contributions are observed in the Mo$3d$ core level spectra, with the higher BE component at 233.3 eV becoming more prominent, especially in samples with higher Pr content. This indicates that in these samples, the crystal symmetry is more susceptible to alteration due to Nb incorporation.

The Pr $3d$ spectra provides information about the Pr^{4+}/Pr^{3+} ratio present in the samples (Figure 4cd). The deconvolution of the spectra, as is common for many lanthanides, reveals several electron satellite structures for the $3d$ and $4d$ ionizations. According to Poggio-Fraccari *et al.* [38], three doublets (blue lines) are assigned to Pr^{4+} (called a''-b'', a-b), and two doublets (green lines) are assigned to Pr^{3+} (called a'-b', a_o-b_o). Therefore, in all cases, both Pr^{4+} and Pr^{3+} species are present. The corresponding atomic ratios are included in Table S2, which shows that the Pr^{4+}/Pr^{3+} ratio becomes smaller as the Pr content increases and remains practically stable after Nb incorporation.
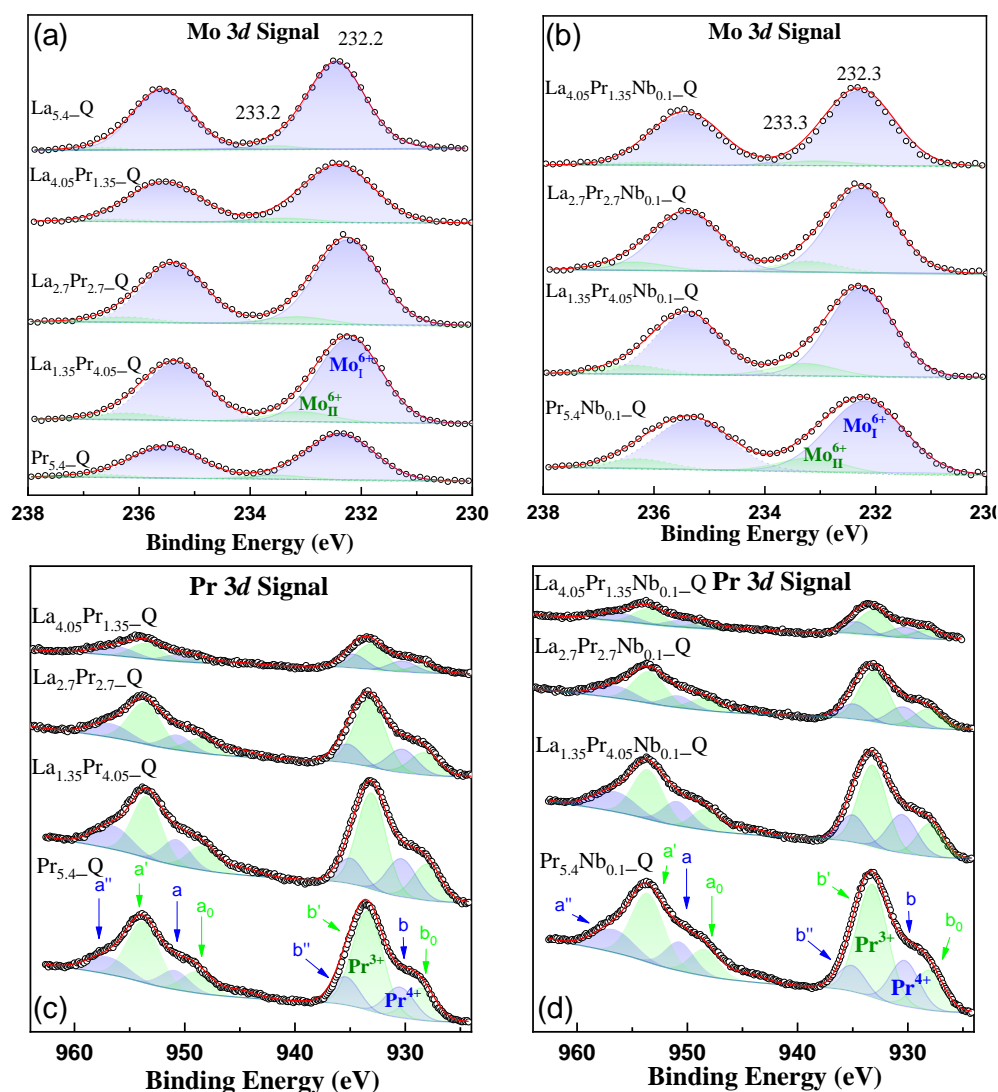
Figure 4. XPS spectra of (a,b) Mo $3d$ and (c,d) Pr $3d$ core levels for the $La_{5.4-x}Pr_xMo_{1-y}Nb_yO_{12-\delta}$ (x = 1.35, 2.7. 4.05, 5.4; y = 0, 0.1) series.

Similar to Pr, the lanthanum spectra are also complex. Figure S2ab shows the La $3d_{5/2}$ component for the different samples with and without Nb-doping. In all cases, four contributions are clearly distinguishable. The main peak, centred at 834.7 eV, is assigned to La^{3+} related to La−Mo−O mixed oxides [39]. The grey dashed lines correspond to satellite peaks. A second much less intense contribution is located at approximately 833.0 eV, observed in all cases. Its intensity is directly related to La and Pr content as well as the presence of Nb. As previously reported, this is assigned to a new chemical environment for La^{3+}, similar to what was observed in the Mo $3d$ signal. Therefore, the proportion of these species increases with both Pr content and after Nb addition.

Finally, the O $1s$ signal, which is much more complex, is also included in Figure S2cd where four contributions are noticeable. For samples without Nb-doping, the $Pr_{5.4}\_Q$ sample shows contributions at 528.5, 530.2, 531.5, and 532.6 eV (Figure S2c), which are associated with a rhombohedral polymorph containing domains of different symmetry as confirmed by TEM studies and previously observed in the Mo and La signals [27]. Specifically, these contributions correspond to the O-lattice related to MoO_3 (~530.9 eV), Pr^{3+} (~531.9 eV) [40], defect oxygen close to oxygen vacancies (531.1–531.4 eV) [41], and surface hydroxyl oxygen species and adsorb oxygen, respectively.

After Pr substitution with La, the contributions at approximately 528.5 and 530.2 eV become more significant due to a partial loss of symmetry (Figure S2d). This change is also observed in the Mo and La signals, as well as the presence of La oxide, which has a BE of 530.5 eV. At higher La

contents, the contribution at 528.5 eV becomes almost negligible as the cubic symmetry is again recovered. Therefore, the La$_{5.4}$Q sample mainly shows two contributions: one at 530.7 eV, associated with the presence of molybdenum, and another at 532.0 eV, corresponding to OH groups and adsorbed oxygen.

On the other hand, the incorporation of Nb into the structure results in a loss of symmetry, regardless of the sample composition, as observed from the Mo and La signals. This is evident from the increase in the O1s signal at 528.5 eV, which is particularly pronounced at higher Pr content.

3.4. Microstructural and Electrical Characterization

SEM images reveal that all ceramic materials are nearly fully dense (Figure 5), with a relative density close to 100%. No detectable fractures, secondary phases, or visible segregations at the grain boundaries are observed for the different materials These findings are further confirmed by EDS analysis, which shows homogenous cation distribution for La$_{2.7}$Pr$_{2.7}$_Q as a representative sample (Figure S3). Similar elemental mappings are observed for the remaining samples, regardless of the composition or cooling rate.
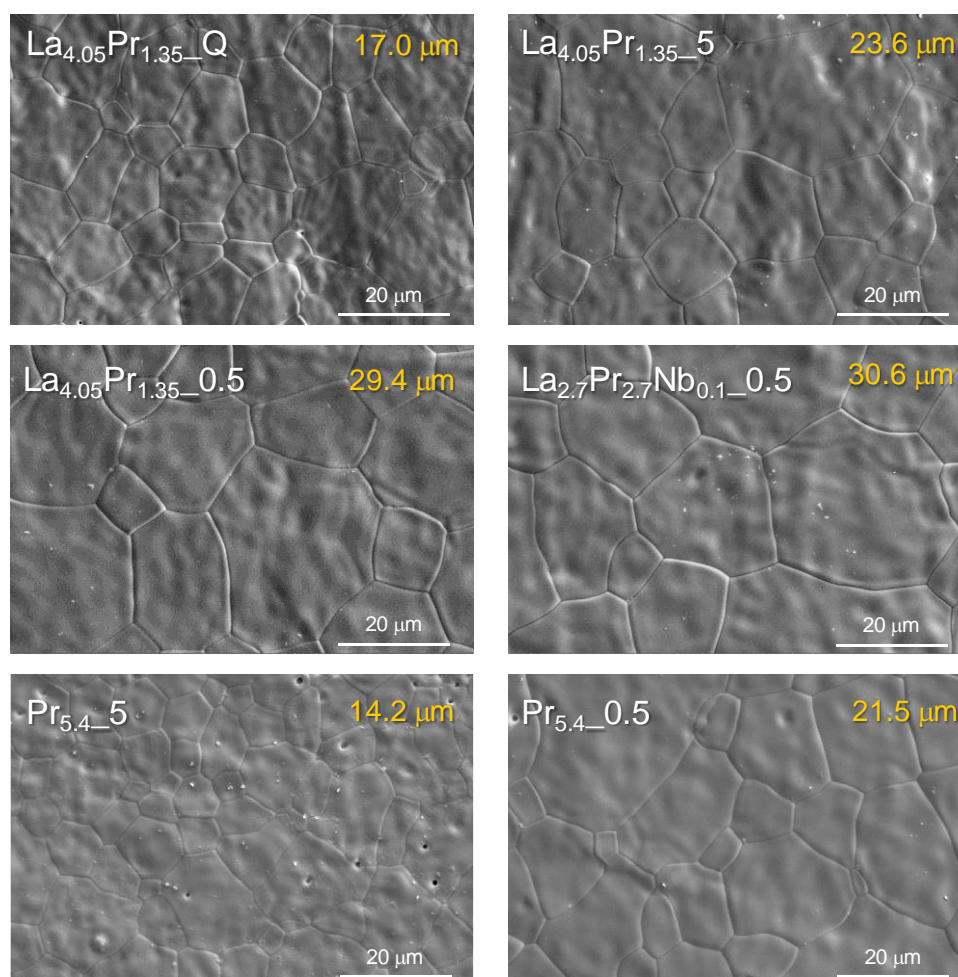

Figure 5. SEM micrographs of the La$_{5.4-x}$Pr$_x$Mo$_{1-y}$Nb$_y$O$_{12-\delta}$ samples (x = 1.35, 2.7. 4.05, 5.4; y = 0, 0.1) sintered at 1500 °C for 1 h and cooled down at different rates. Average grain size is denoted at the top right of the images.

The analysis of the average particle size reveals that, in general, higher Pr contents lead to a decrease in grain size, with values of 23.6, 20.7 and 14.2 µm for La$_{4.05}$Pr$_{1.35}$_5, La$_{2.7}$Pr$_{2.7}$_5 and Pr$_{5.4}$_5, respectively. A similar trend was observed in a previous work, where molybdates containing smaller lanthanides exhibited reduced average grain sizes [27]. On the other hand, Nb-doping does not appear to have a significant effect on the particle size. Additionally, the average grain size increases as the cooling rate decreases, with values of 11.8, 14.2 and 21.5 µm for Pr$_{5.4}$_Q, Pr$_{5.4}$_5 and Pr$_{5.4}$_0.5,

respectively. This increase is attributed to the longer dwelling time at 1500 ºC for the lower cooling rates, which allows for more extensive grain growth.

Figure 6 shows the impedance spectra for $La_{2.7}Pr_{2.7}\_Q$ and $Pr_{5.4}\_Q$ as representative examples of the series, both quenched and measured under dry/wet N_2 and wet 5% H_2–Ar (similar plots are obtained for the other compositions). The plots reveals the presence of two different contributions: one corresponding to bulk conduction within the grain interior, characterized by capacitances on the order of 10^{-12} F cm^{-1}, and the other associated with electrode processes, characterized by capacitances on the order of 10^{-2} F cm^{-1} [21]. These plots can be accurately fitted using an $(R_bQ_b)(R_eQ_e)$ equivalent circuit model, where the subscripts b and e denote the bulk and electrode processes, respectively (inset Figure 6). It is important to note that no grain boundary contribution to the overall conductivity was observed, likely due to the large average grain size and the absence of secondary phases, as confirmed by SEM images.
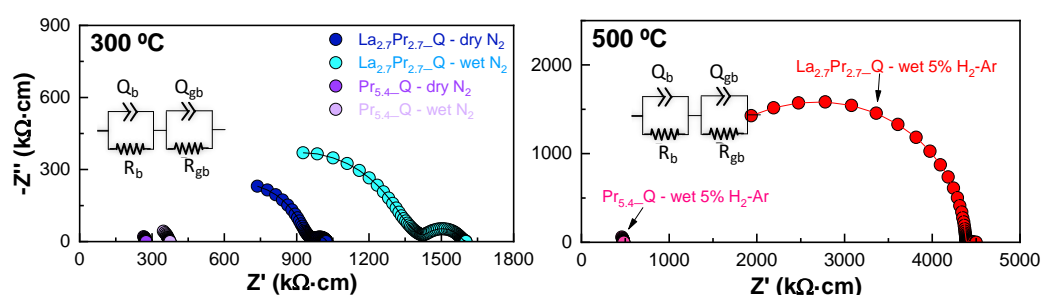
Figure 6. Representative impedance spectra of $La_{2.7}Pr_{2.7}0.5$ and $Pr_{5.4}Q$ under (top) dry/wet N_2 at 300 °C and (bottom) 5% H_2–Ar gases at 500 °C. The equivalent circuit used to fit the spectra are show in the insets.

Notably, under wet N_2 conditions, the bulk resistance increases compared to a dry N_2, which contrasts with findings in other studies of La, Sm and Gd-based molybdates [21,22,27], where water incorporation into the oxide vacancies enhanced proton conductivity. However, this behaviour is similar to that observed in $Nd_{5.4}MoO_{11.1}$ [27] and in other Nd-containing proton conductors, such as Nd-doped $La_2Ce_2O_7$ [42], where an increase in p-type conductivity was observed with increasing Nd content. This phenomenon was attributed to Nd^{3+} being less prone to be oxidation to Nd^{4+}, similar to the Pr^{3+}/Pr^{4+} pairs observed here. Therefore, the presence of a significant p-type electronic contribution to the overall conductivity in Pr-containing molybdates suggests a competition between O_2 and H_2O for absorption into the oxide vacancies, which reduces the proton conductivity.

The Arrhenius plots (Figure 7) and Table S3 clearly demonstrate that in a N_2 atmosphere, the conductivity increases significantly with higher Pr contents, ranging from 0.17 to 204.4 mS cm^{-1} for $La_{5.4}\_Q$ and $Pr_{5.4}\_Q$, respectively, at 700 ºC. This increase is attributed to the presence of the Pr^{4+}/Pr^{3+} pair, which enhances the electronic contribution to the overall conductivity. Furthermore, the activation energies decrease significantly as the Pr content increases, with values of 1.04(1), 0.37(1) and 0.26(1) eV for $La_{5.4}\_Q$, $La_{2.7}Pr_{2.7}\_Q$ and $Pr_{5.4}\_Q$, respectively, in the 750-550 ºC temperature range under dry N_2. This behaviour suggests a transition in the transport properties, from predominantly ionic conduction for samples with low Pr-content to predominantly electronic conduction in those with high Pr-content. Therefore, the mixed ionic/electronic conductivity of these materials can be tailored through appropriate Pr-substitution.
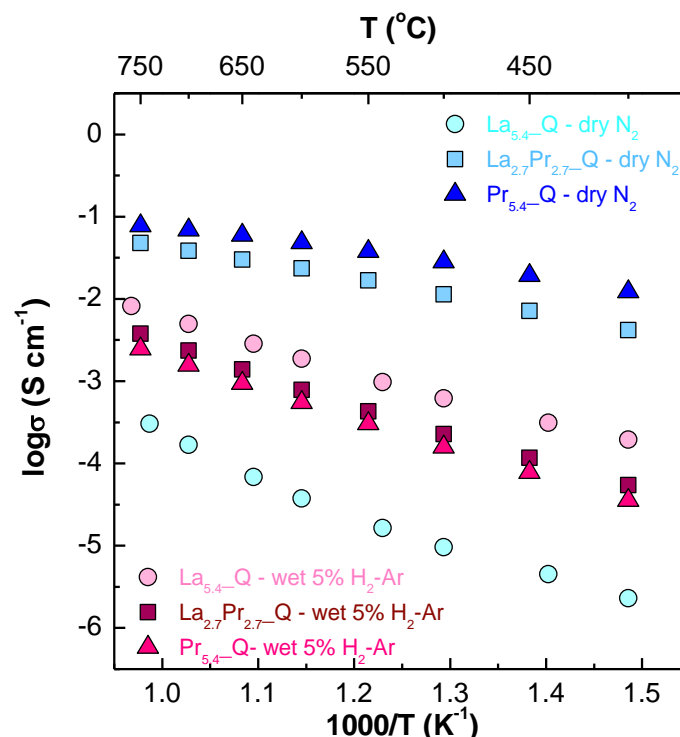
Figure 7. Arrhenius plots of $La_{5.4}Q$, $La_{2.7}Pr_{2.7}Q$ and $Pr_{5.4}Q$ sintered at 1500 ℃ for 1 h and cooled down by quenching under dry N_2 and wet 5% H_2-Ar atmospheres.

Interestingly, Nb-doped samples generally exhibit increased conductivity, which is attributed to the generation of additional oxide vacancies resulting from this aliovalent substitution (Figure S4 and Table S3). This effect is more pronounced at lower temperatures and in wet atmospheres, where the ionic conductivity (oxide and proton) dominates due to the enhanced ability of the increased number of oxide vacancies to incorporate water. For example, in the case of $La_{2.7}Pr_{2.7}\_Q$ and $Pr_{5.4}\_Q$, the conductivity values in wet N_2 at 400 ℃ increase from 3.0 and 15.3 mS cm^{-1}, respectively, to 3.6 and 16.3 mS cm^{-1} for the corresponding Nb-doped samples under the same conditions, further demonstrating the beneficial effect of Nb-doping.

Under reducing conditions, a different behaviour is observed, with a significant drop in conductivity for the praseodymium containing samples. This is attributed to the nearly complete reduction of Pr^{4+} to Pr^{3+}, resulting in a significant decrease of the electronic conductivity. Additionally, the conductivity decreases with increasing Pr content, with values of 5.0, 2.3 and 1.6 mS cm^{-1} for $La_{5.4}\_Q$, $La_{2.7}Pr_{2.7}\_Q$ and $Pr_{5.4}\_Q$, respectively. This decrease is primarily attributed to the shrinkage of the unit cell volume caused by the size difference between La^{3+} (1.16 Å) and Pr^{3+} (1.13 Å), which hinders the ionic conduction pathways. This volume shrinkage effect is also reflected in the slightly higher activation energies. In particular, $La_{5.4}\_Q$ has an activation energy of 0.70(1) eV, while $La_{2.7}Pr_{2.7}\_Q$ and $Pr_{5.4}\_Q$ exhibit values of 0.79(1) and 0.76(1) eV, respectively. Furthermore, Nb-doping enhances the electrical properties under reducing conditions, particularly at high temperatures. For instance, conductivity values for $Pr_{5.4}\_Q$ and $Pr_{5.4}Nb_{0.1}\_Q$ are 1.6 and 3.5 mS cm^{-1}, respectively, at 700 ℃ (Table S3). It is also worth noting that a significant drop in electronic conductivity for samples with high Pr-content may be less relevant in fuel cell and electrolyzer operational conditions, where the membranes typically operate under an oxygen concentration gradient.

4. Conclusions

For the first time, lanthanum and praseodymium molybdates with the general formula $La_{5.4-x}Pr_xMo_{1-y}Nb_yO_{12-\delta}$ (x= 1.35, 2.7, 4.05, 5.4; y= 0, 0.1) have been successfully synthesized using the freeze-drying precursor method. The compounds were sintered at 1500 ℃ and subsequently cooled at

different rates. The quenched samples exhibited cubic symmetry due to the inherent disorder in the crystal lattice at high temperatures. Slower cooling rates, combined with high Pr content, resulted in cubic symmetry due to the minor distortion induced by the smaller ionic radius of Pr compared to La. In contrast, compositions with lower Pr content stabilized the R1 rhombohedral polymorph. However, TEM studies indicates a more complex local structure depending on Pr content, with a gradual transformation from defect-free cubic fluorite structure at high Pr-content to one with numerous local defects, and finally a modulated arrangement or domains embedded in the cubic phase at low Pr content.

Scanning electron microscopy (SEM) and energy-dispersive X-ray spectroscopy (EDS) analyses revealed that the synthesized samples are dense and exhibit a homogeneous cation distribution, regardless of the preparation conditions or the crystal structure adopted.

The highest conductivity values were observed in a N_2 atmosphere, which can be attributed to the presence of mixed Pr^{4+}/Pr^{3+} cations. However, the proton conductivity deceased due to an increase in p-type electronic contribution. Furthermore, in a reducing atmosphere (5% H_2-Ar), the conductivity of Pr-substituted samples drastically decreased due to the reduction of Pr^{4+} to Pr^3, highlighting the importance of the material composition and operating atmospheres on the conducting properties of these materials for different electrochemical applications.

Supplementary Materials: The following supporting information can be downloaded at: www.mdpi.com/xxx/s1, Figure S1: XRD patterns for $La_{5.4-x}Pr_xMo_{1-y}Nb_yO_{12-\delta}$ samples (x = 0, 1.35, 2.7. 4.05, 5.4; y = 0, 0.1) heated at 1500 °C and cooled down by quenching. Symmetry of the samples is labelled is displayed within the figure; Figure S2: XPS spectra of (a,b) O 1s and (c,d) La 3$d_{5/2}$ core levels for the $La_{5.4-x}Pr_xMo_{1-y}Nb_yO_{12-\delta}$ (x = 0, 1.35, 2.7. 4.05, 5.4; y = 0, 0.1) series; Figure S3: SEM micrograph and EDS mappings for La, Pr and Mo for the $La_{2.7}Pr_{2.7}MoO_{12-\delta}Q$ sample; Figure S4: Arrhenius plots of $La_{5.4-x}Pr_xMo_{0.9}Nb_{0.1}O_{12-\delta}$ samples (x = 0, 2.7. 5.4) sintered at 1500 °C for 1 h and cooled down by quenching under dry N_2 and wet 5% H_2-Ar atmospheres.

Author Contributions: Conceptualization: J.M.P-V. and E.R.L; methodology: J.M.P-V., D.M-L. and E.R.L.; investigation: A. S-C., J.M.P-V., L.d.S.-G., J.Z.-G., A.I-M., and J.C-V.; formal analysis: J.M.P.-V., A.I-M, J.C-V, and D.M.-L.; validation: J.M.P.-V, D.M.-L. and E.R.L.; visualization: A. S-C., J.M.P-V. and D.M.-L.; project administration: J.M.P-V., D.M-L. and E.R.L.; writing—original draft: A. S-C. and J.M.P-V.; writing—review and editing: J.M.P.-V., E.R.L. and D.M.-L.

Conflicts of Interest: The authors declare no conflicts of interest.

References

1. Kim, D.; Lee, T. K.; Han, S.; Jung, Y.; Lee, D. G.; Choi, M.; Lee, W. Advances and challenges in developing protonic ceramic cells. Mater. Today Energy 2023, 36, 101365. https://doi.org/10.1016/j.mtener.2023.101365.

2. Cheng, S.; Li, X.; Huang, X.; Ling, Y.; Liu, S.; Li, T. Hydrogen separation via proton conducting ceramic membranes: A review. *Int. J. Hydrogen Energy* **2024**, *70*, 654−665. https://doi.org/10.1016/j.ijhydene.2024.05.181.

3. Dou, J.; Wang, S.; Yao, Z. Mixed protonic–electronic conducting ceramic membranes for hydrogen separation: A review on recent advances in structure optimization and preparation. *Sep. Purif. Technol.* **2025**, *355*, 129582. https://doi.org/10.1016/j.seppur.2024.129582

4. Zhang, W.; Liu, M.; Gu, X.; Shi, Y.; Deng, Z.; Cai, N. Water electrolysis toward elevated temperature: advances, challenges and frontiers. *Chem. Rev.* **2023**, *123*, 7119–7192. https://doi.org/10.1021/acs.chemrev.2c00573

5. Vignesh, D.; Rout, E. Technological challenges and advancement in proton conductors: a review. *Energy Fuels* **2023**, *37*, 5, 3428–3469. https://doi.org/10.1021/acs.energyfuels.2c03926

6. Matkin, D. E.; Starostina, I. A.; Hanif, M. B.; Medvedev, D. A. Revisiting the ionic conductivity of solid oxide electrolytes: A technical review. *J. Mater. Chem. A* **2024**, *12*, 25696-25714. https://doi.org/10.1039/d4ta03852e

7. Hossain, M. K.; Biswas, M. C.; Chanda, R. K.; Rubel, M. H. K.; Khan, M. I.; Hashizume, K. A review on experimental and theoretical studies of perovskite barium zirconate proton conductors. *Emergent Mater.* **2021**, *4*, 999–1027. https://doi.org/10.1007/s42247-021-00230-5

8. Mohd Rashid, N. L.; Abdul Samat, A.; Jais, A. A.; Somalu, M. R.; Muchtar, A.; Baharuddin, N. A.; Wan Isahak, W. N. R. Review on zirconate-cerate-based electrolytes for proton-conducting solid oxide fuel cell. *Ceramics International* **2019, 45**, 6605–6615. https://doi.org/10.1016/j.ceramint.2019.01.045

9. Danilov, N. A.; Starostina, I. A.; Starostin, G. N.; Kasyanova, A. V.; Medvedev, D. A.; Shao, Z. Fundamental understanding and applications of protonic Y- and Yb-Coped Ba(Ce,Zr)O$_3$ perovskites: state-of-the-art and perspectives. *Adv. Energy Mater.* **2023**, *13*, 2302175. https://doi.org/10.1002/aenm.202302175

10. Fang, S.; Brinkman, K. S.; Chen, F. Hydrogen permeability and chemical stability of Ni–BaZr$_{0.1}$Ce$_{0.7}$Y$_{0.1}$Yb$_{0.1}$O$_{3-\delta}$ membrane in concentrated H$_2$O and CO$_2$. *J. Membr. Sci.* **2014**, *467*, 85–92. https://doi.org/10.1016/j.memsci.2014.05.008

11. Yang, C.; Cao, W.; Shen, Q.; Li, J.; Wang, L.; Yao, W.; Liang, Y.; Wang, K. Electrochemical properties of Sr-doped La$_{2-x}$Sr$_x$Ce$_2$O$_{7-\delta}$ hydrogen separation membrane. *Int. J. Hydrogen Energy* **2024**, *63*, 720–730. https://doi.org/10.1016/j.ijhydene.2024.03.108

12. Zamudio-García, J.; Porras-Vázquez, J. M.; Canales-Vázquez, J.; Cabeza, A.; Losilla, E. R.; Marrero-López, D. Relationship between the structure and transport properties in the Ce$_{1-x}$La$_x$O$_{2-x/2}$ system. *Inorg. Chem.* **2019**, *58*, 9368–9377. https://doi.org/10.1021/acs.inorgchem.9b01104

13. Norby, T.; Magrasó, A. On the development of proton ceramic fuel cells based on Ca-doped LaNbO$_4$ as electrolyte. *J. Power Sources* **2015**, *282*, 28–33. https://doi.org/10.1016/j.jpowsour.2015.02.02

14. Zayas-Rey, M. J.; dos Santos-Gómez, L.; Porras-Vázquez, J. M.; Losilla, E. R.; Marrero-López, D. Evaluation of Lanthanum Tungstates as Electrolytes for Proton Conductors Solid Oxide Fuel Cells. *J. Power Sources* **2015**, *294*, 483–493.https://doi.org/10.1016/j.jpowsour.2015.06.102

15. Gil, V.; Gurauskis, J.; Kjølseth, C.; Wiik, K.; Einarsrud, M.-A. Hydrogen permeation in asymmetric La$_{28-x}$W$_{4+x}$O$_{54+3x/2}$ membranes. *Int. J. Hydrogen Energy* **2013**, *38*, 3087−3091. https://doi.org/10.1016/j.ijhydene.2012.12.105

16. Escolástico, S.; Solís, C.; Scherb, T.; Schumacher, G.; Serra, J.M. Hydrogen separation in La$_{5.5}$WO$_{11.25-\delta}$ membranes, *J. Membr. Sci.* **2013**, *444*, 276−284. http://dx.doi.org/10.1016/j.memsci.2013.05.005

17. Gil, V.; Gurauskis, J.; Einarsrud, M.-A. Asymmetric supported dense lanthanum tungstate membranes. *J. Eur. Ceram. Soc.* **2014**, *34*, 3783−3790. http://dx.doi.org/10.1016/j.jeurceramsoc.2014.06.019

18. Vøllestad, E.; Vigen, C.K.; Magrasó, A.; Haugsrud, R. Hydrogen permeation characteristics of La$_{27}$Mo$_{1.5}$W$_{3.5}$O$_{55.5}$. *J. Membr. Sci.* **2014**, *461*, 81−88. http://dx.doi.org/10.1016/j.memsci.2014.03.011

19. Chen, Y.; Liao, Q.; Li, Z.; Wang, H.; Wei, Y.; Feldhoff, A.; Caro, J. A CO$_2$-stable hollow-fiber membrane with high hydrogen permeation flux. *AIChE J*. **2015**, *61*, 1997−2007. http://dx.doi.org/10.1002/aic.14772

20. Polfus, J.M.; Xing, W.; Fontaine, M.L.; Denonville, C.; Henriksen, P.P.; Bredesen, R. Hydrogen separation membranes based on dense ceramic composites in the La$_{27}$W$_5$O$_{55.5}$−LaCrO$_3$ system. *J. Membr. Sci.* **2015**, *479*, 39−45. http://dx.doi.org/10.1016/j.memsci.2015.01.027

21. López-Vergara, A.; Porras-Vázquez, J.M.; Infantes-Molina, A.; Canales-Vázquez, J.; Cabeza, A.; Losilla, E.R.; Marrero-López, D. Effect of preparation conditions on the polymorphism and transport properties of La$_{6-x}$MoO$_{12-\delta}$ (0 ≤ x ≤ 0.8). *Chem. Mater.* **2017**, *29*, 6966–6975. https://doi.org/10.1021/acs.chemmater.7b02481

22. López-Vergara, A.; Vizcaíno-Anaya, L.; Porras-Vázquez, J.M.; Baldinozzi, G.; dos Santos-Gómez, L.; Canales-Vazquez, J.; Marrero-López, D.; Losilla, E.R. Unravelling crystal superstructures and transformations in the La$_{6-x}$MoO$_{12-\delta}$ (0.6 ≤ x ≤ 3.0) series: a system with tailored ionic/electronic conductivity. *Chem. Mater*. **2020**, *32*, 7052–7062. https://dx.doi.org/10.1021/acs.chemmater.0c02673

23. Dan Vu, T.; Krichen, F.; Barré, M.; Coste, S.; Jouanneaux, A.; Suard, E.; Fitch, A.; Goutenoire, F. Ab-initio structure determination of La$_{34}$Mo$_8$O$_{75}$ using powder X-ray and neutron diffraction data. *Cryst. Growth Des*. **2019**, *19*, 6074–6081. http://dx.doi.org/10.1021/acs.cgd.8b01552

24. López-Vergara, A.; Porras-Vázquez, J.M.; Vøllestad, E.; Canales-Vázquez, J.; Losilla, E.R.; Marrero-López, D. Metal-Doping of $La_{5.4}MoO_{11.1}$ Proton Conductors: Impact on the Structure and Electrical Properties, *Inorg. Chem*. **2018**, *57*, 12811−12819. https://doi.org/10.1021/acs.inorgchem.8b02010

25. Savvin, S.N.; Shlyakhtina, A.V.; Kolbanev, I.V.; Knotko, A.V.; Belov, D.A.; Shcherbakova, L.G.; Nuñez, P. Zr-doped samarium molybdates — potential mixed electron–proton conductors. *Solid State Ionics* **2014**, *262*, 713−718. https://doi.org/10.1016/j.ssi.2014.01.031

26. Shlyakhtina, A.V.; Savvin, S.N.; Lyskov N.V.; Kolbanev, I.V.; Karyagina, O.K.; Chernyak, S.A.; Shcherbakova, L.G.; Nuñez, P. Polymorphism in the family of $Ln_{6-x}MoO_{12-\delta}$ (Ln = La, Gd–Lu; x = 0, 0.5) oxygen ion- and proton-conducting materials. *J. Mater. Chem. A* **2017**, *5*, 7618−7630. https://doi.org/10.1039/C6TA09963G

27. Rubio-Vives, R.; Porras-Vázquez, J.M.; dos Santos-Gómez, L.; Zamudio-García, J.; Infantes-Molina, A.; Canales-Vazquez, J.; Marrero-López, D.; Losilla, E.R. Impact of the lanthanide size on the polymorphism and electrical properties of $Ln_{5.4}MoO_{11.1}$ (Ln = Nd, Sm and Gd). *Ceramics International* **2023**, *49*, 12805–12813. http://dx.doi.org/10.1016/j.ceramint.2022.12.146

28. Chen, D.J.; Ran, R.; Zhang, K.; Wang, J.; Shao, Z.P. Intermediate-temperature electrochemical performance of a polycrystalline $PrBaCo_2O_{5+\delta}$ cathode on samarium-doped ceria electrolyte. *J. Power Sources* **2009**, *188*, 96. http://dx.doi.org/10.1016/j.jpowsour.2008.11.045

29. Jin, F.J.; Shen, Y.; Wang, R.; He, T.M. Double-perovskite $PrBaCo_{2/3}Fe_{2/3}Cu_{2/3}O_{5+\delta}$ as cathode material for intermediate-temperature solid-oxide fuel cells. *J. Power Sources* **2013**, *234*, 244. http://dx.doi.org/10.1016%2Fj.jpowsour.2013.01.172

30. Zayas-Rey, M.J.; dos Santos-Gómez, L.; Marrero-López, D.; León-Reina, L.; Canales-Vázquez, J.; Aranda, M.A.G.; Losilla, E.R. Structural and Conducting Features of Niobium-Doped Lanthanum Tungstate, $La_{27}(W_{1-x}Nb_x)_5O_{55.55-\delta}$. *Chem. Mater*. **2013**, *25*, 448−456. http://dx.doi.org/10.1021/cm304067d

31. X'Pert High Score Plus Program, version 3.0e, PANalytical B.V.: Amelo, The Netherlands, **2012**.

32. Larson, A.C.; von Dreele, R.B. GSAS Program; Report LA-UR-86748, Los Alamos National Lab, **1994**.

33. Multipak v9.3 Software. Data Reduction Software for AES & XPS; Physical Electronics, **2010**

34. Digital Micrograph, Version 3.22.1461.0; Gatan: Pleasanton, CA.

35. Abrantes, J.C.C. U.I.D.M. Estereología, ESTG, Polytechnic Institute of Viana do Castelo: Viana do Castelo, Portugal, **1998**.

36. Johnson, D. ZView: A Software Program for IES Analysis, Version 2.9c, Scribner Associates, Inc.: Southern Pines, NC, **2005**.

37. Amsif, M.; Magrasó, A.; Marrero-López, D.; Ruiz-Morales, J.C.; Canales-Vázquez, J.; Núñez, P. Mo-substituted lanthanum tungstate $La_{28-y}W_{4+y}O_{54+\delta}$: a competitive mixed electron−proton conductor for gas separation membrane applications. *Chem. Mater*. **2012**, *24*, 3868−3877. https://doi.org/10.1021/cm301723a

38. Poggio-Fraccari, E.; Baronetti, G.; Mariño, F. Pr^{3+} surface fraction in CePr mixed oxides determined by XPS analysis. *J. Electron Spectrosc*. **2018**, *222*, 1−4. https://doi.org/10.1016/j.elspec.2017.11.003.

39. Escolástico, S.; Somacescu, S.; Serra, J.M. Tailoring mixed ionic−electronic conduction in H_2 permeable membranes based on the system $Nd_{5.5}W_{1-x}Mo_xO_{11.25-\delta}$. *J. Mater. Chem. A* **2015**, *3*, 719−731. https://doi.org/10.1039/C4TA03699A

40. Oni, B.A.; Tomomewo, O.S.; Sanni, S.E.; Ibegbu, A.J.; Joseph, R. Ni catalysts modified with mesoporous silica support: The role of Pr_2O_3 and MgO on the methanation of CO_2. *Molecular Catalysis* 2024, **553**, 113774. https://doi.org/10.1016/j.mcat.2023.113774

41. Kim, J.-H.; Kim, J.-E.; Kim, H.-M.; Jeong, D.-W. Characteristics and performance of the $Co-CeO_2$ catalyst as a function of the promoter (La, Pr, and Zr) used in high temperature water gas shift reaction. *Int. J. Hydrogen Energy* **2021**, *46*, 12981−12991. https://doi.org/10.1016/j.ijhydene.2021.01.147

42. Kalland, L.-E.; Løken, A.; Bjørheim, T.S.; Haugsrud, R.; Norby, T. Structure, hydration, and proton conductivity in 50% La and Nd doped CeO_2 – $La_2Ce_2O_7$ and $Nd_2Ce_2O_7$ – and their solid solutions. *Solid State Ionics* **2020**, *354*, 1154. https://doi.org/10.1016/j.ssi.2020.115401 Author 1, A.B.; Author 2, C. Title of Unpublished Work. *Abbreviated Journal Name* year, *phrase indicating stage of publication (submitted; accepted; in press)*.